Detection and characterization of transport barriers in complex flows via ridge extraction of the finite time Lyapunov exponent field

Carmine Senatore*,† and Shane D. Ross

Department of Engineering Science and Mechanics, Virginia Tech, Blacksburg, VA 24061, U.S.A.

SUMMARY

This paper proposes an algorithm to detect and characterize ridges in the finite time Lyapunov exponent (FTLE) field obtained from a continuous dynamical system or flow. These ridges represent time-dependent separatrices of the flow and are also called Lagrangian coherent structures (LCS). LCS have been demonstrated to be an effective way to analyze realistic time-chaotic flows, although they can be quite complex. Therefore, in order to exploit the information that LCS can provide it is important to locate and characterize these structures in a systematic way. This can be accomplished by interpreting the FTLE as a height field and detecting the LCS as ridges of this graph. Methodologies developed in the image processing framework are integrated with dynamical system inspired approaches in order to characterize ridge strength and location. The main novel contribution of the proposed algorithm is a scheme to connect sets of points into curves or surfaces (rather than distributions of points around a ridge axis) and classify these curves or surfaces using a dynamical systems measure of strength. This approach provides the capability to track ranked LCS in space and time. The results are presented for a simple analytical model and noisy LCS from realistic three-dimensional geophysical fluid data. Copyright © 2010 John Wiley & Sons, Ltd.

1. INTRODUCTION

Lagrangian coherent structures (LCS) have emerged as a useful tool to identify important features in dynamical flows, including but not limited to fluid flows (see, e.g. [1–14]). Within the phase space, or in the case of fluids, the position space, LCS are considered to be codimension one sets of high stretching, or more formally, have been defined [6] as ridges in a finite time Lyapunov exponent (FTLE) field. As regions of greatest attraction, repulsion, or shearing, they act as important transport barriers, organizing the overall transport structure of a flow. For some systems, FTLE ridges can be determined by visual inspection of the field. For other systems, this field can be very complex, warranting the development of methods for LCS extraction [15]. In addition, a systematic method for not only extracting but also characterizing LCS when many are present is useful for tracking and identifying individual features that may merit further analysis.

The aim of this paper is to present a tool for the extraction and characterization of LCS exploiting concepts developed in the image processing and dynamical system framework. Given the definition

---

*Correspondence to: Carmine Senatore, 77 Massachusetts Ave. Room 35-135A, Cambridge, MA 02139, U.S.A.
†E-mail: senator@mit.edu

of LCS as ridges of the FTLE field (a scalar field) [6, 8], the problem is restated as the analysis of an image.

Ridge detection algorithms are deeply rooted into computer science practices. In particular, the analysis of fingerprint images is a field where accurate ridge detection is crucial: the minutiae detection and matching process necessarily relies on fingerprint image pattern recognition. O'Gorman and Nickerson [16] proposed a filter design for enhancing fingerprint images; a smoothing filter oriented along the ridge direction was developed. Maio and Maltoni [17] introduced a technique based on a ridge line following algorithm that follows the image ridge lines until a termination or a bifurcation occurs. Zhu *et al.* [18] proposed a scheme for systematically estimating fingerprint ridge orientation and segmenting fingerprint image by means of evaluating the correctness of the ridge orientation based on neural network. Jiang *et al.* [19] presented minutiae detection procedure based on adaptive tracing the gray-level ridge of the fingerprint image with piecewise linear lines of different lengths. Algorithms for fingerprint comparison, based on minutiae matching, are presented in [20–22].

The application of ridge detection algorithms for LCS analysis is a relatively recent field of study. Researchers are primarily focused on visualization methodologies [23–25]; the LCS location is calculated through ridge detection algorithms but no characterization of the structure is provided. Shi *et al.* [26] adopt a path-line integral convolution approach to calculate the LCS location and uncover the dynamical information of flow transport. Pekiert and Sadlo [27] present an algorithm able to detect ridge points without using eigenvalues; this approach can have a beneficial impact on the computation time.

The aforementioned methodologies are attractive for visualization but none of them provide characterization or ranking of the dynamical structures (i.e. the LCS). The algorithms developed in the pattern recognition environment are tailored to minutiae analysis and do not consider the strength of the ridges. On the other hand, the algorithms which have flourished in the dynamical system field are primarily concerned with visualization issues and do not provide ridge classification.

We develop and demonstrate a reliable multi-scale, multi-step method for LCS detection which can extract features even in the presence of the non-smoothing effects of noise. Furthermore, we characterize the detected features in terms of their strength per unit length. The novelty of the proposed algorithm resides on the capability to consistently group together ridge points into ranked LCS curves, which can be tracked in space and time.

The method is illustrated on a simple analytically determined (but noisy) image and on atmospheric flow data, where LCS have the interpretation of important atmospheric transport barriers.

2. FINITE TIME LYAPUNOV EXPONENT

The FTLE (the maximum is understood) can be calculated as:

$$\sigma_{t_0}^{\tau}(\mathbf{x}) = \frac{1}{|\tau|} \ln \left\| \frac{\mathrm{d}\phi_{t_0}^{t_0+\tau}(\mathbf{x})}{\mathrm{d}x} \right\|, \tag{1}$$

where $\phi_{t_0}^{t_0+\tau}(\mathbf{x})$ is the flow map which maps the particle from its initial position $\mathbf{x}(t_0) = \mathbf{x}_0$ at time t_0 to its position $\mathbf{x}(t) = \phi_{t_0}^{t+\tau}(\mathbf{x})$ at time $t_0+\tau$. The FTLE value for a particle is assigned to its location at time t_0, not $t_0+\tau$. The matrix norm in Equation (1) is $\|A\| = \sqrt{\lambda_{\max}(A^*A)}$, where A^* is the transpose of the square matrix A and $\lambda_{\max}(M)$ denotes the maximum eigenvalue of the matrix M.

The FTLE measures the maximum exponential growth rate (over a finite time duration τ) of the distance between particle trajectories starting near a reference particle trajectory at time t_0. From now on the dependence of σ on t_0 and τ will be understood.

The FTLE can be calculated from analytical, experimental or calculated velocity fields but the applications are not limited to fluid flows. One can think of the phase portrait of a mechanical system as a velocity field. In this perspective it is possible to calculate the FTLE from known

trajectories of the system that might be available through experiments [13]. The ridges of the FTLE field are structures called LCS that have the property of organizing and separating phase space regions of qualitatively different types of motion. The FTLE has been calculated through a standard algorithm that relies on computing trajectories on a structured or unstructured mesh [14] and performs finite differencing of final positions [6].

Briefly, one calculates the final position $\mathbf{x}(t_0+\tau)=\phi_{t_0}^{t_0+\tau}(\mathbf{x})$ of each grid point $\mathbf{x}$ at an initial time t_0 when advected by the flow for a duration τ. To obtain this, each point is advected with a fourth-order Runge–Kutta integration algorithm using the provided (possibly time-dependent) velocity data. Once all points are mapped from their initial positions, $\mathbf{x}(t_0)$, to their final positions, $\mathbf{x}(t_0+\tau)$, the gradient of the flow map, $\phi_{t_0}^{t_0+\tau}$, has to be computed. We choose points in the grid that are initially close, so the gradient of the flow map can be computed through finite differences.

3. RIDGE DEFINITION

Eberly [28] proposes two definitions of ridges: watershed ridge and height ridge. The former is inspired by geomorphological considerations while the latter is derived from differential geometry.

With the watershed approach one has to analyze the whole graph in order to detect peaks, pits, passes, contour and slope lines. From this information one can form a set of points called a hill or dale. Then, the slope lines that separate hills are called course lines while the ones separating dales are called ridge lines. This approach requires overall consideration on the whole graph and is global in nature.

On the other hand, the height ridge definition relies on differential geometry quantities calculated at each point and so is local in nature. In this paper, the latter definition is adopted because it is more natural for computational implementation. A height ridge in n-dimension can be defined, following [28], as:

Definition 1
Let $f \in C^2(\mathbb{R}^n, \mathbb{R})$. Let $\lambda_i, 1 \leqslant i \leqslant n$, be the eigenvalues of the Hessian of f, $\nabla^2 f$, ordered such that $\lambda_1 \leqslant \cdots \leqslant \lambda_n$. Let $\mathbf{v}_i, 1 \leqslant i \leqslant n$, be corresponding unit-length (column) eigenvectors. A point $\mathbf{x}$ is a d-dimensional ridge point if $\mathbf{x}$ is a generalized local maximum point of type d with respect to $V = [\mathbf{v}_1 \cdots \mathbf{v}_{n-d}]$. Since $V^*\nabla^2 f(\mathbf{x})V = \text{diag}(\lambda_1, \ldots, \lambda_{n-d})$ and the eigenvalues are ordered, the test for a ridge point reduces to $V^*\nabla f(\mathbf{x}) = \mathbf{0}$ and $\lambda_{n-d}(\mathbf{x}) < 0$.

A generalized local maximum point of type d is defined as follows:

Definition 2
Let $f \in C^2(\mathbb{R}^n, \mathbb{R})$. For a given d with $0 \leqslant d < n$ and an $n \times (n-d)$ matrix V of rank $n-d$, the point $\mathbf{x}$ is a generalized local maximum point of type d with respect to V if $V^*\nabla f(\mathbf{x}) = \mathbf{0}$ and $V^*\nabla^2 f(\mathbf{x})V < 0$.

Definition 1 is for general n, d and f. If one set $f = \sigma$, $n = 2$ and $d = 1$ (i.e. one-dimensional ridges of the FTLE field viewed as a graph of $\mathbb{R}$ over $\mathbb{R}^2$), the definition can be reduced to the following test:

$$\nabla \sigma(\mathbf{x}) \cdot \mathbf{v}_{\min}(\mathbf{x}) = 0,$$
$$\lambda_{\min}(\mathbf{x}) < 0. \tag{2}$$

A point $\mathbf{x}$ is a ridge point if it satisfies these conditions which have the following interpretation: the first derivative in the direction transverse to the ridge axis is zero (i.e. a local maximum/minimum) and the second derivative in the transverse direction is negative (i.e. the curvature is negative when the field is at a local maximum in the transverse direction). The vector $\mathbf{v}_{\min}$ in (2) is the eigenvector corresponding to the minimum eigenvalue $\lambda_{\min}$ of the Hessian, $\nabla^2 \sigma(\mathbf{x})$.

To illustrate this definition the function $\sigma(x, y) = -x^2$ is evaluated on the domain $[-1, 1] \times [-2, 2]$ as shown in Figure 1. For $x = 0$ this function has $\nabla \sigma(\mathbf{x}) \cdot \mathbf{v}_{\min}(\mathbf{x}) = [-2x^2, 0] \cdot [1, 0] = 0$ and
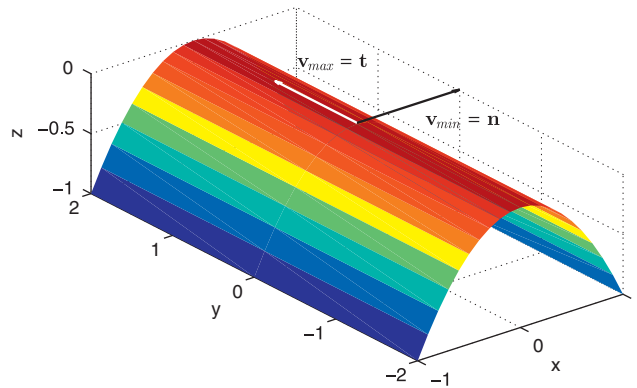
Figure 1. Function $\sigma(x, y) = -x^2$ plotted over the domain $[-1, 1] \times [-2, 2]$. Two eigen-vectors for the point (0,0) are presented.

$\lambda_{\min}(\mathbf{x}) = -2 < 0$. Therefore the ridge is along $x = 0$. The eigenvector associated with the smallest eigenvalue of the Hessian matrix of $\sigma(x, y)$ is normal to the axis of the ridge while the other eigenvector is tangential with the axis of the ridge. Given this interpretation, from now on $\mathbf{v}_{\min}$ will be referred as $\mathbf{n}$ and $\mathbf{v}_{\max}$ as $\mathbf{t}$. The algorithm starts from these basic considerations of differential geometry in order to detect the features in the FTLE field, considered as a (scalar-valued or gray-scale) image.

4. DETECTION ALGORITHM

The algorithm for detecting and classifying a ridge consists of five steps: scale-space representation and ridge point detection, dynamical sharpening, connecting ridge points into ridge curves, choice of best scale and classification of ridges (by, e.g. barrier strength).

4.1. Scale-space representation and ridge point detection

In image processing it is common to analyze an image in its *scale-space* [23, 29, 30]. This operation consists of a convolution of the function $\sigma \in C^2(\mathbb{R}^2, \mathbb{R})$ with a Gaussian kernel $g \in C^2(\mathbb{R}^2, \mathbb{R})$:

$$\sigma_a(\mathbf{x}) = g(\mathbf{x}; a) * \sigma(\mathbf{x}), \tag{3}$$

where a determines the value of the *scale* and the Gaussian kernel $g \in C^2(\mathbb{R}^2, \mathbb{R})$ is given by:

$$g(x, y; a) = \frac{1}{2\pi a^2} e^{-\frac{x^2 + y^2}{2a^2}}. \tag{4}$$

The convolution produces smoother images. This is necessary for two reasons: image features exist as meaningful entities only over certain ranges of scales (see Reference [31]) and since the FTLE field is often calculated from noisy data sets, it requires smoothing.

The parameter a determines the scale of the smoothing and plays a key role in the detection of well-defined ridges. In the discussed applications, the strongest ridges usually have the same scale and will be completely revealed for some value of a. In Figure 2 an example of smoothing at different scales is shown. It is clear how the smoothing acts as a filter; ultimately the convolution corresponds to a product in the frequency domain (i.e. the convolution theorem). For $a = 0$ one will have $\sigma_0(\mathbf{x}) = g(\mathbf{x}; 0) * \sigma(\mathbf{x}) = \sigma(x)$, i.e. the convolution returns the original image.

Ten possible scale-spaces are set and the ridge points satisfying Equation (2) are detected at every scale. The parameter a can vary continuously from 0 to ∞ but only ten scales (at which we expect the ridge to be enhanced significantly) are analyzed in order to speed up the computation. Section 4.4 will explain how the best scale is selected.

The choice of a depends on the transversal dimension of the ridges under investigation: one has to consider an average ridge thickness and choose the scales keeping in mind that the Gaussian
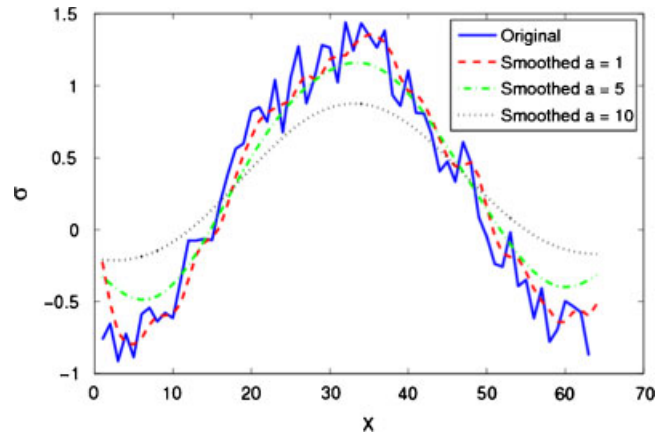
Figure 2. A ridge given by $\sigma(x) = \cos(x/10) + \varepsilon(x)$, where $\varepsilon(x)$ is random (white) noise. Transversal sections of the ridge smoothed at three different scales are presented. It is clear that for some value of a the smoothing is not enough to highlight the profile of the ridge while for others it excessively flattens the profile.

filter highlights features in a domain of $[6\sqrt{a}, 6\sqrt{a}]$. This is due to the fact that $\sqrt{a}$ represents the standard deviation and in a normally distributed process (i.e. the Gaussian bell) 99.7% of the data is within $6\sqrt{a}$.

4.2. Dynamical sharpening

The first step produces a set of points that are often scattered around the axis of the ridge (this is due to the noisy nature of the original plot [5], and to the numerical approximation on the threshold for the derivatives). This might not be a relevant issue if one only desires to plot the ridge position but if one wants to connect the ridge points in order to create a curve, it is necessary to have an ordered sequence of points lying on the axis of the ridge. A connected curve of points is useful for labeling and characterizing ridges, as shown in a later section.

To get rid of this problem the notion that a ridge acts as an attractor for the gradient dynamical system [15] is exploited:

$$\frac{d\mathbf{x}_0}{ds} = \nabla\sigma_a(\mathbf{x}_0), \tag{5}$$

where s is the arclength along the gradient lines of $\sigma_a(\mathbf{x}_0)$. Equation (5) is integrated using as initial position the ridge points calculated during the previous step of the algorithm. This step produces a set of points accumulated along the ridge axis as schematically shown in the central panel of Figure 3. Since the elevation of the ridge is not constant the gradient is not zero at the top of the ridge. For this reason the effectiveness of this strategy relies on stopping the computation of Equation (5) when the solution $\mathbf{x}_0(s)$ reaches the crest of the ridge (see [15] for details).

4.3. Connection of calculated points

Since ridges are contiguous structures, the detected points are connected in order to create curves. Candidate point $\mathbf{P}_2$ is put in the same ridge set of point $\mathbf{P}_1$ if the following conditions are satisfied:

$$|\mathbf{P}_2 - \mathbf{P}_1| \leqslant d_0, \tag{6}$$

$$|\sigma_a(\mathbf{P}_2) - \sigma_a(\mathbf{P}_1)| \leqslant h_0, \tag{7}$$

$$\arccos\left(\frac{\mathbf{t}_2 \cdot \mathbf{t}_1}{|\mathbf{t}_2||\mathbf{t}_1|}\right) \leqslant \frac{\pi}{4}, \tag{8}$$

$$\arccos\left(\frac{\mathbf{t}_1 \cdot (\mathbf{P}_2 - \mathbf{P}_1)}{|\mathbf{t}_1||\mathbf{P}_2 - \mathbf{P}_1|}\right) \leqslant \frac{\pi}{4}, \tag{9}$$
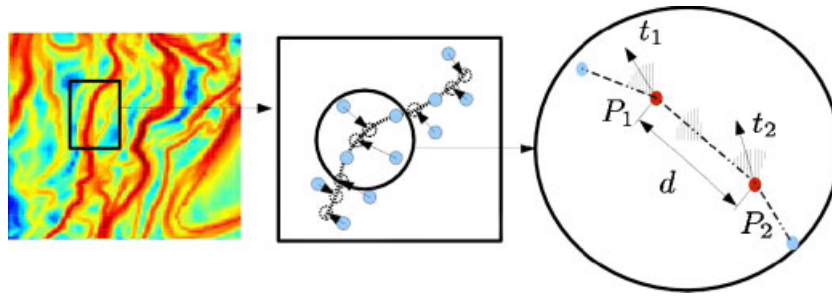
Figure 3. Main steps of the algorithm. From the initial image (left panel) the ridge points are calculated and aggregated toward the ridge axis (central panel). Thereafter, the points are appropriately connected (right panel) in order to create curves.

where $\mathbf{t}_1$ and $\mathbf{t}_2$ are the eigenvectors tangent to the ridge at $\mathbf{P}_1$ and $\mathbf{P}_2$, respectively. Equation (6) states that the two points must be closer than a threshold d_0. Equation (7) checks whether the difference in height between the two points is lower than a threshold h_0. Equation (8) tests whether the angle between $\mathbf{t}_1$ and $\mathbf{t}_2$ is smaller than $\pi/6$. This comes from the assumption that the ridge curves are continuous and differentiable and therefore properties change smoothly throughout the curve, in particular, there should be no sharp corners to the curves. Finally, Equation (9) is a check on the alignment of the vector connecting $\mathbf{P}_1$ and $\mathbf{P}_2$ with the tangent vector at the point $\mathbf{P}_1$. If these four conditions are satisfied the points $\mathbf{P}_1$ and $\mathbf{P}_2$ are saved in the same ridge set as illustrated in the right panel of Figure 3.

4.4. Choice of best scale

Selecting the right scale is a crucial step. In this paper, a procedure similar to that proposed in [31] is followed; several scales are swept and based on an appropriate performance measure the scale that optimizes this measure is picked. Since our goal is to create sequences of ordered points (i.e. curves representing the LCS location) the obvious approach is to use the length of the ridge as a measure. For every scale the length of the detected features is calculated and the scale that has produced the longest features is selected.

Figure 4 presents the results obtained for a sample ridge with random noise. As this example illustrates, the ridge is detected in its entirety at one scale, while at a lower scale, it shows a series of disconnected ridge lines.

4.5. Classification of ridges

At this stage, ridge lines have been obtained but are not ranked yet. Besides the ridge length, it is interesting to ascertain which barrier is dynamically stronger.

Different options for ridge strength have been proposed in the literature [6, 28, 31, 32]. Being a ridge a locus of points where the FTLE field—a measure of the stretch-ratio of the flow— is locally maximal, from the dynamical point of view, a ridge is stronger if the separation of particles suddenly drops on its two sides.

Thus, the ridge strength is mainly related to the lower-in-norm principal curvature. The result for the flux across an LCS obtained by Shadden [33] and based on the lower-in-norm curvature is adopted. At a particular point along an LCS (ridge), the flux of particles across the LCS is:

$$\frac{\mathrm{d}L}{\mathrm{d}t} = \frac{\mathbf{t} \cdot \nabla \sigma}{\mathbf{n} \cdot \nabla^2 \sigma \mathbf{n}} \left[\mathbf{t} \cdot \left(\frac{\partial \mathbf{n}}{\partial t} - J \mathbf{n} \right) \right], \tag{10}$$

where J is the Jacobian matrix of the velocity field. For an extensive discussion of Equation (10) we suggest [33]. The term in the square brackets is related to the difference in the rotation rate of the LCS from the rotation rate induced by the velocity field and is discarded for this analysis for the sake of simplicity. In flows, even geophysical flows such as the one considered here, where local vorticity can change suddenly, this term may not be negligible. Given this caveat, we consider
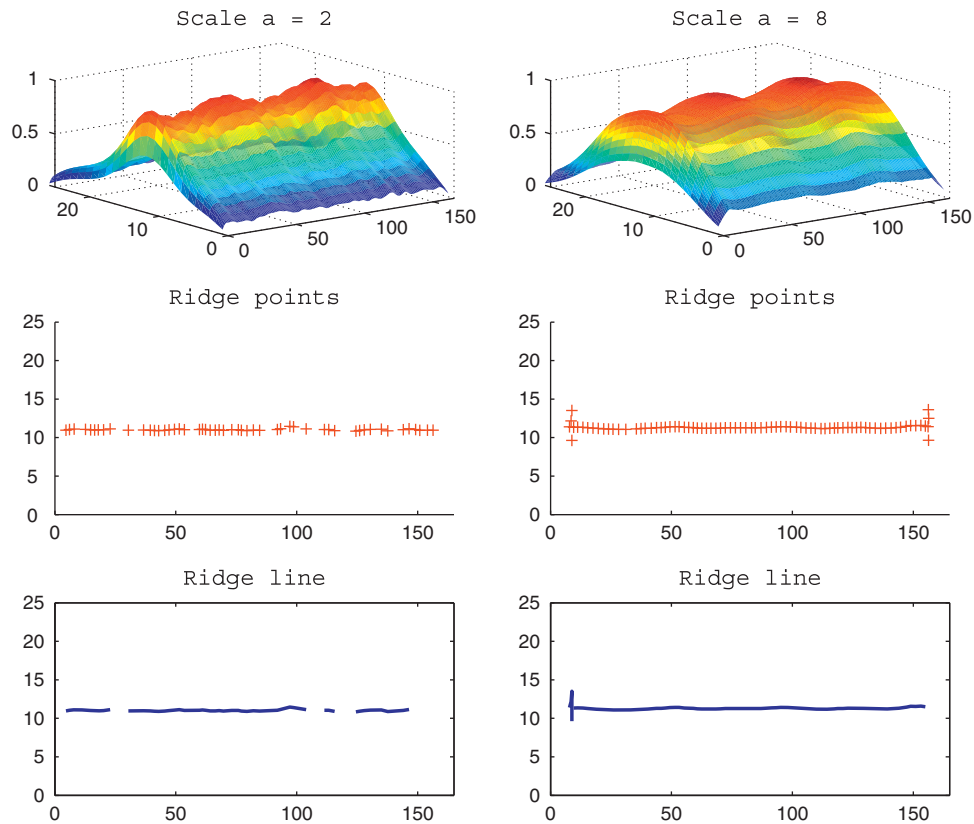
Figure 4. In the top row is a sample ridge at two scales (left and right column). In the central row are the ridge points detected after the dynamical sharpening. In the bottom row are the ridge lines obtained after the connection of calculated points. For $a=2$ the detected ridge line is disconnected; only for $a=8$ we obtain a connected ridge.

the first term of the flux equation (10). The numerator of this term tends to vanish in the presence of strong ridges because σ is almost constant along a ridge (e.g. it is strictly constant for a time-independent flow). The denominator of the first term is related to the greater-in-norm curvature associated with the ridge point and is maximized (in norm) for sharper ridges. Therefore, the first term tends to zero for a well-defined and visually sharp ridge.

We adopt the following measure of the ridge strength at a point $\mathbf{x}$ along a ridge as,

$$S \equiv 1 - \left| \frac{\mathbf{t} \cdot \nabla \sigma}{\mathbf{n} \cdot \nabla^2 \sigma \mathbf{n}} \right|. \tag{11}$$

In this formulation the strongest ridges have strength close to 1. For a time-independent flow the FTLE field would have well-defined ridges with constant value. This would lead to $\nabla \sigma(\mathbf{x})=0$ and $S=1$. In realistic time-chaotic flows, the FTLE does not have constant height ridges and so the denominator of Equation (11) plays a role in determining the strength of the ridge. The height or length of the ridge would not represent an adequate measure of strength because they do not give the sharpness of the ridge (which, e.g. captures how non-uniform is the particle separation).

5. RESULTS

Results obtained on a sample picture are presented first. An image presenting three ridges with different curvature was created. The crest of the ridge has a sinusoidal shape and random noise is
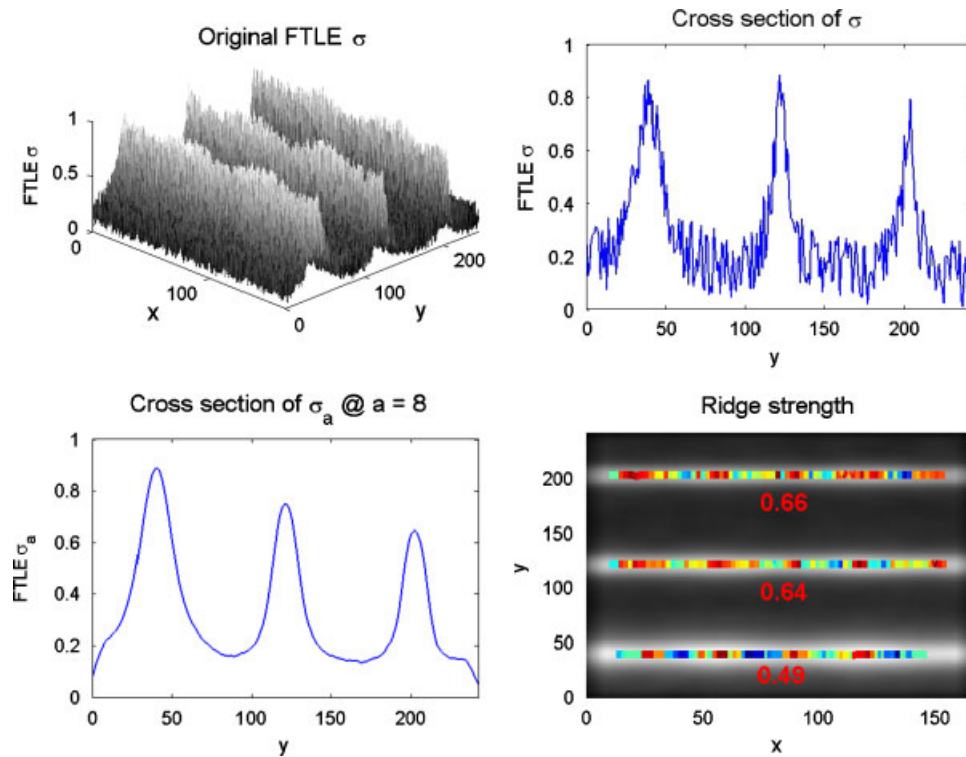
Figure 5. In the top-left panel a sample image with three ridges. The top-right panel shows a section of the ridges, they have been created in such a way that the curvature is different for each one of them. In the bottom-left panel the profile of the ridge after smoothing is presented while in the bottom-right panel the final output of the algorithm is shown: the ridges are plotted over the original image and the average strengths are listed. Along each ridge, the differential strength is shown: red corresponds to high strength, blue to low strength (Color online). The x, y axis are in number of grid points.

added in order to simulate a worst-case scenario. The FTLE has the following analytical expression:

$$\sigma(x, y) = \frac{\sin(x)}{1 + ky^2} + \varepsilon(x, y) \tag{12}$$

where k is a parameter that influences the curvature and $\varepsilon(x, y)$ is the random noise.

The results follow our expectations: the method is able to detect the ridges in the height field and the measure of the strength is consistent with the imposed curvature. The bottom-right panel of Figure 5 shows the detected ridges: hotter colors (red) correspond to higher strength and vice versa (cold colors, blue, to weaker features, color online); the average strength of the ridge points are printed as well, and can be considered a measure of the strength of the ridge itself, allowing for rank ordering of ridges by strength.

Following the ridge line there are sections where the ridge is stronger and sections where it is weaker. This is consistent with the definition of the strength we give because where the crest is flat (top or bottom of the sine curve) the denominator of Equation (10) vanishes.

The next example is taken from an FTLE field calculated from an analytical velocity field. A double gyre flow is considered as an exemplar of the types of flow of interest. The 2-D velocity field $V(x, y, t) = (u(x, y, t), v(x, y, t))$ of the double gyre is defined analytically as:

$$u = -\pi B \sin(\pi h(x)) \cos(\pi y), \tag{13}$$

$$v = \pi B \cos(\pi h(x)) \sin(\pi y) \frac{dh}{dx}, \tag{14}$$
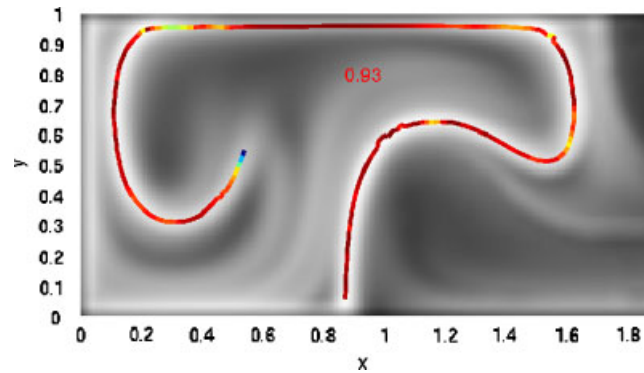
Figure 6. LCS extracted from the double gyre flow. Only the strongest ridge (with average strength 0.93) is shown. In this case the crest of the ridge has almost constant elevation along the feature resulting in a strong LCS.

where $h(x,t) = c(t)x^2 + b(t)x$, $c(t) = \gamma \sin(\omega t)$, $b(t) = 1 - 2\gamma \sin(\omega t)$, and where B is related to the amplitude of the velocity, γ measures the amplitude of the oscillation of the gyre (i.e. the shifting of the saddle $(1,0)$ during the motion) and ω is the frequency of the system. This flow is studied over the domain $[0,2] \times [0,1]$ while the other parameters are set as follows: $B = 0.1$, $\gamma = 0.1$, $\omega = 2\pi/10$ and $\tau = 10$. This type of flow shows a single dominant LCS separating the two regions of the domain. Figure 6 shows how the algorithm is able to catch the winding nature of the LCS.

The next example is a data set containing realistic data, particularly a geophysical flow.

We make use of an archived assimilated meteorological model provided by the National Oceanic and Atmospheric Administration (NOAA). The North American Mesoscale (NAM) data set, which includes a North American grid of three-dimensional winds (u, v, w) with a temporal resolution of 3 hours and spatial resolution of approximately 12 km [34] is adopted. The FTLE field is computed over a portion of the northeastern United States, which includes the towns of Blacksburg, Virginia (where the main Virginia Tech campus is located) and Ithaca, New York (Cornell University). The horizon time τ is set to two days. In Figure 7, two snapshots of the FTLE field taken on 27 May 2008 and assuming isobaric flow on a pressure level of 975 mb (corresponding to an altitude of approximately 200 m above the ground level) are presented. These snapshots are of interest because they highlight the presence of two strong LCS extending in the north-south direction. These two atmospheric transport barriers delineate a moving north-south transport corridor, which may be relevant for transport of aerobiota, including airborne plant pathogens and other invasive species [35–38]. The video http://www.esm.vt.edu/sdross/movies/BB_Cornell.mov http://www.esm.vt.edu/sdross/movies/BB_Cornell.mov (files can be downloaded from our site) shows the full sequence of images in animated format.

To highlight the power of LCS we add to the plot three boxes of drifters roughly on either side of the two LCS labeled A and B in Figure 7. The LCS behave as dynamical structures that organize and bound the motion of the flow surrounding them (see the drifters). Notice that the features A and B can be identified through time and have roughly the same average strength at both times. In this realistic case, detecting the true ridges is more difficult than for an analytically known flow. For the sake of visualization we only show the features with average strength greater than 0.3, omitting weaker ridges. The algorithm successfully detects the longest and strongest ridges. These plots reveal the complexity of a real scenario. Critical situations that lead to difficulties are where there is a local maximum (i.e. where principal directions are not defined), the features have sharp turns (i.e. where the principal directions have great variation), and where features bifurcate as well as come together. All of these difficulties arise due mostly to the richness of the underlying fluid flow.

As a final example, wind data from the NOAA data set is exploited to illustrate how it is possible to use the algorithm to create LCS surfaces in a 3-D flow. In the fully three-dimensional flow of the atmosphere, the LCS are two-dimensional undulating sheets; see Figure 8. In a 3-D atmospheric
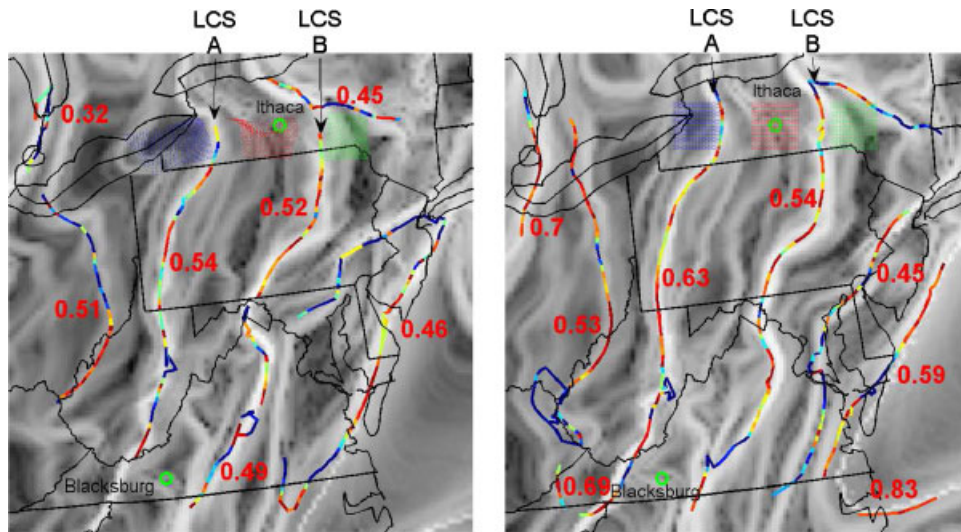
Figure 7. Ridges calculated from two FTLE snapshots taken on 27 May 2008. The snapshot on the right is 6 h after the one on the left. The velocity field data corresponds to wind data at pressure level of 975 mb provided by NOAA. Two strong LCS labeled 'LCS A' and 'LCS B' are highlighted. These two features bound an air mass that roughly runs north-south and it includes both Blacksburg, Virginia and Ithaca, New York. The barrier property of the LCS is emphasized by drawing three sets of drifters that follow the dynamical barriers represented by the LCS. See http://www.esm.vt.edu/sdross/movies/BB_Cornell.mov http://www.esm.vt.edu/sdross/movies/BB_Cornell.mov (files can be downloaded from our site) to view the full sequence of images in animated format.
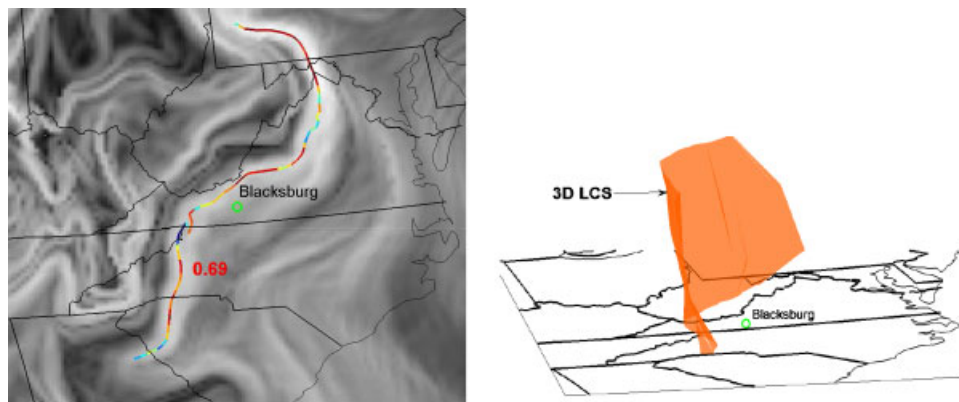
Figure 8. In the left panel an LCS detected over the town of Blacksburg,VA at a pressure level of 975 mb in mid-April 2007. Three LCS at different pressure levels have been detected and connected together in order to create the 3-D LCS sheet shown in the right panel. The vertical scale has been greatly exaggerated and we note that the LCS is advancing to the right. See http://www.esm.vt.edu/~sdross/movies/3D_LCS.mov http://www.esm.vt.edu/sdross/movies/3D_LCS.mov (files can be downloaded from our site) to view the full sequence of images in animated format.

setting, one can assume that over short times the flow is organized into roughly horizontal 2-D layers [23]. We analyze the winds at a pressure level of 975 mb and note that there is an LCS passing over the town of Blacksburg, Virginia. We make the assumption that the flow is quasi-two-dimensional at each altitude (i.e. pressure level) and then look for LCS at the next available pressure level. Our assumption is confirmed by the presence of similar LCS at pressure levels 975, 950, 925 and 900 mb. Then the LCS location is calculated at every altitude and the 2-D ridges are connected in order to represent a 3-D feature. Figure 8 shows, in the left panel an LCS detected at 975 mb, and in the right panel a 3-D LCS obtained by the connection of features at different

pressure levels. These atmospheric transport barriers may play a role in the population structure of airborne microbes, controlling movement between geographically dispersed habitats [37, 39]. Additional work to test these hypotheses is underway and will be the subject of another paper. Here, we wish only to point out that 2-D sheets can be extracted and tracked through time.

6. CONCLUSIONS

An algorithm for LCS extraction and characterization was proposed and implemented.

We introduced a measure of the strength of the ridge from a dynamical systems perspective, and demonstrated the ability to calculate both differential strength along an LCS as well as average strength. We proposed a methodology to track the LCS as curves (in 2-D) and surfaces (in 3-D) and not merely as an unstructured set of points or as a contour field and demonstrated this ability in an atmospheric flow.

There is room for improvement in the computational implementation in order to make it faster and more efficient. The choice of the right scale-space remains an important point in order to produce meaningful results. The proposed method introduces an almost automatic choice of the scale: if one knows the transversal dimension of the average ridge, and the grid spacing it is easy to find a range of scales over which to search. In fact, this is the only task left to the user.

A possible improvement of the code is to apply a B-spline interpolation of the FTLE field in order to more accurately calculate whether the conditions of Equation (2) are met. Nevertheless, an inadequate choice of scale would heavily counteract any advantages of the interpolation, and therefore proper scale choice is primary.

The algorithm does not take into account the possibility of a bifurcating ridge: in the case of a bifurcation, the LCS is recognized as two separate features. Further work is warranted in this area in order to rationally connect diverging or converging ridge points or different ridge lines, to characterize features that bifurcate or join as time goes on.

Future work can address the problem of tracking the ridges through time. Understanding LCS evolution in a flow of arbitrary time-dependence is crucial and the possibility of automatically detecting the strongest and most persistent structures would be relevant to emerging applications which employ LCS for analysis (e.g. [9, 10, 12, 13]).

REFERENCES

1. Haller G, Yuan G. Lagrangian coherent structures and mixing in two-dimensional turbulence. *Physica D* 2000; **147**:352–370.
2. Haller G. Finding finite-time invariant manifolds in two-dimensional velocity fields. *Chaos* 2000; **10**:99–108.
3. Haller G. Distinguished material surfaces and coherent structures in 3D fluid flows. *Physica D* 2001; **149**:248–277.
4. Haller G. Lagrangian structures and the rate of strain in a partition of two-dimensional turbulence. *Physics of Fluids* 2001; **13**:3365–3385.
5. Haller G. Lagrangian coherent structures from approximate velocity data. *Physics of Fluids* 2002; **13**:3365.
6. Shadden SC, Lekien F, Marsden JE. Definition and properties of Lagrangian coherent structures: mixing and transport in two-dimensional aperiodic flows. *Physica D* 2005; **212**:271–304.
7. Lekien F, Coulliette C, Mariano AJ, Ryan EH, Shay LK, Haller G, Marsden JE. Pollution release tied to invariant manifolds: a case study for the coast of Florida. *Physica D* 2005; **210**:1–20.
8. Lekien F, Shadden SC, Marsden JE. Lagrangian coherent structures in *n*-dimensional systems. *Journal of Mathematical Physics* 2007; **48**:065404.
9. Shadden SC, Taylor CA. Characterization of coherent structures in the cardiovascular system. *Annals of Biomedical Engineering* 2008; **36**:1152–1162.
10. Senatore C, Ross SD. Fuel-efficient navigation in complex flows. *Proceedings of 2008 American Control Conference*, Seattle, WA, 2008; 1244–1248.
11. Tallapragada P, Ross SD. Particle segregation by Stokes number for small neutrally buoyant spheres in a fluid. *Physical Review E* 2008; **78**:036308.
12. Gawlik ES, Marsden JE, Du Toit PC, Campagnola S. Lagrangian coherent structures in the planar elliptic restricted three-body problem. *Celestial Mechanics and Dynamical Astronomy* 2009; **103**(3):227–249.
13. Tanaka ML, Ross SD. Separatrices and basins of stability from time series data: an application to biodynamics. *Nonlinear Dynamics* 2009; **58**(1–2):1–21.

14. Lekien F, Ross SD. The computation of finite-time Lyapunov exponents on unstructured meshes and for non-Euclidean manifolds. *Chaos* 2010; **20**:017505.
15. Mathur M, Haller G, Peacock T, Ruppert-Felsot JE, Swinney HL. Uncovering the Lagrangian skeleton of turbulence. *Physical Review Letters* 2007; **98**:144502.
16. O'Gorman L, Nickerson JV. An approach to fingerprint filter design. *Pattern Recognition* 1989; **22**(1):29–38.
17. Maio D, Maltoni D. Direct gray-scale minutiae detection in fingerprints. *IEEE Transactions on Pattern Analysis and Machine Intelligence* 1997; **19**(1):27–40.
18. Zhu E, Yin J, Hu C, Zhang G. A systematic method for fingerprint ridge orientation estimation and image segmentation. *Pattern Recognition* 2006; **39**:1452–1472.
19. Jiang X, Yau WY, Ser W. Detecting the fingerprint minutiae by adaptive tracing the gray-level ridge. *Pattern Recognition* 2001; **34**:999–1013.
20. Xiao Q, Raafat H. Fingerprint image postprocessing: a combined statistical and structural approach. *Pattern Recognition* 1991; **24**(10):985–992.
21. Farina A, Kovács-Vajna ZM, Leone A. Fingerprint minutiae extraction from skeletonized binary images. *Pattern Recognition* 1999; **32**:877–889.
22. He Y, Tian J, Li L, Chen H, Yang X. Fingerprint matching based on global comprehensive similarity. *IEEE Transactions on Pattern Analysis and Machine Intelligence* 2006; **28**(6):850–862.
23. Garth C, Gerhardt F, Tricoche X, Hagen H. Efficient computation and visualization of coherent structures in fluid flow applications. *IEEE Transactions on Visualization and Computer Graphics* 2007; **13**(6):1464–1471.
24. Sadlo F, Peikert R. Efficient visualization of Lagrangian coherent structures by filtered AMR ridge extraction. *IEEE Transactions on Visualization and Computer Graphics* 2007; **13**(6):1456–1463.
25. Sahner J, Weinkauf T, Teuber N, Hege H. Vortex and strain skeletons in Eulerian and Lagrangian frames. *IEEE Transactions on Visualization and Computer Graphics* 2007; **13**(5):980–990.
26. Shi K, Theisel H, Weinkauf T, Hege H, Seidel H. Finite time transport structures of flow fields. *IEEE Pacific Visualization Symposium*, Kyoto, Japan, 4–7 March 2008.
27. Peikert R, Sadlo F. Height ridge computation and filtering for visualization. *IEEE Pacific Visualization Symposium*, Kyoto, Japan, 4–7 March 2008.
28. Eberly D. *Ridges in Image and Data Analysis*. Kluwer Academic Publishers: Dordrecht, 1996.
29. Florack L. *Image Structure*. Kluwer Academic Publishers: Dordrecht, 1997.
30. Lindeberg T. Scale-space theory: A basic tool for analysing structures at different scales. *Journal of Applied Statistics* **21**:225–270.
31. Lindeberg T. Edge detection and ridge detection with automatic scale selection. *International Journal of Computer Vision* 1998; **30**(2):117–156.
32. Subirana-Vilanova JB, Sung KK. Multi-scale vector-ridge-detection for perceptual organization without edges. *Technical Report*, Massachussets Institute of Technology, 1992.
33. Shadden SC. A dynamical systems approach to unsteady systems. *Ph.D. Thesis*, California Institute of Technology, 2003.
34. National Oceanic and Atmospheric Administration. Nomads Data Access, 12km North American Mesoscale (nam) dataset. Available from: http://nomads.ncdc.noaa.gov/data.php [June 2009].
35. Aylor DE. Spread of plant disease on a continental scale: role of aerial dispersal of pathogens. *Ecology* 2003; **84**:1989–1997.
36. Isard SA, Gage SH, Comtois P, Russo JH. Principles of the atmospheric pathway for invasive species applied to soybean rust. *BioScience* 2005; **55**(10):851–861.
37. Schmale DG, Shields EJ, Bergstrom GC. Night-time spore deposition of the Fusarium head blight pathogen gibberella zeae. *Canadian Journal Plant Pathology* 2006; **28**:100–108.
38. Newton PK, Ross SD. Chaotic advection in the restricted four-vortex problem on a sphere. *Physica D* 2006; **223**:36–53.
39. Boehm MT, Aylor DE. Lagrangian stochastic modeling of heavy particle transport in the convective boundary layer. *Atmospheric Environment* 2005; **39**:4841–4850.